Research Article

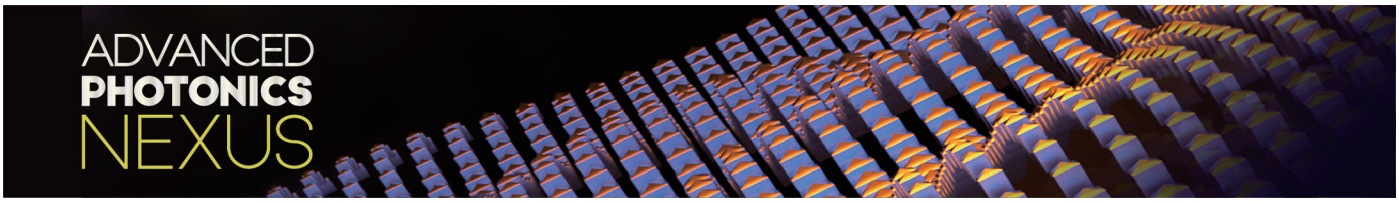

Highly sensitive mid-infrared upconversion detection based on external-cavity pump enhancement

Xiaohan Liu,[a] Kun Huang,[a,b,c,*] Wen Zhang,[a] Ben Sun,[a] Jianan Fang,[a] Yan Liang,[d] and Heping Zeng[a,b,e,f]
[a]East China Normal University, State Key Laboratory of Precision Spectroscopy, Shanghai, China
[b]Chongqing Institute of East China Normal University, Chongqing Key Laboratory of Precision Optics, Chongqing, China
[c]Shanxi University, Collaborative Innovation Center of Extreme Optics, Taiyuan, China
[d]University of Shanghai for Science and Technology, School of Optical Electrical and Computer Engineering, Shanghai, China
[e]Shanghai Research Center for Quantum Sciences, Shanghai, China
[f]Chongqing Institute for Brain and Intelligence, Guangyang Bay Laboratory, Chongqing, China

Abstract. Sensitive mid-infrared (MIR) detection is in high demand in various applications, ranging from remote sensing, infrared surveillance, and environmental monitoring to industrial inspection. Among others, upconversion infrared detectors have recently attracted increasing attention due to their advantageous features of high sensitivity, fast response, and room-temperature operation. However, it remains challenging to realize high-performance passive MIR sensing due to the stringent requirement of high-power continuous-wave pumping. Here, we propose and implement a high-efficiency and low-noise MIR upconversion detection system based on pumping enhancement via a low-loss optical cavity. Specifically, a single-longitudinal-mode pump at 1064 nm is significantly enhanced by a factor of 36, thus allowing for a peak conversion efficiency of up to 22% at an intracavity average power of 55 W. The corresponding noise equivalent power is achieved as low as 0.3 fW/Hz$^{1/2}$, which indicates at least a 10-fold improvement over previous results. Notably, the involved single-frequency pumping would facilitate high-fidelity spectral mapping, which is particularly attractive for high-precision MIR upconversion spectroscopy in photon-starved scenarios.

Keywords: infrared detection; single-photon detection; upconversion detection.

Received Apr. 28, 2024; revised manuscript received May 8, 2024; accepted for publication May 13, 2024; published online May 27, 2024.

[DOI: 10.1117/1.APN.3.4.046002]

1 Introduction

The mid-infrared (MIR) spectrum not only contains abundant fingerprinting vibrational transitions for many molecules but also covers multiple windows with high transmittance in the Earth's atmosphere. Ultrasensitive MIR detection is of great interest in scientific, industrial, and defense fields, such as trace analysis, pollution monitoring, biomedical diagnosis, remote sensing, and free-space communications.[1] Compared with visible or near-infrared bands, the MIR spectral region offers additional thermal information, which is particularly favorable for target recognition and object tracking in low-light conditions.[2] In these aforementioned applications, it is of great interest to improve the MIR detection sensitivity for addressing the needs in photon-scarce scenarios, for instance, long-distance operation, covert surveillance, or phototoxicity-free observation.[3,4] However, commercial MIR photodetectors based on narrow-bandgap semiconductors such as HgCdTe, InSb, or PbSe usually suffer from high dark noise and low response speed, which results in a typical noise equivalent power (NEP) at the level of pW/Hz$^{1/2}$.[2,5] Recently, superconducting nanowire single-photon detectors have demonstrated impressively broad spectral responses up to far-infrared wavelengths, albeit with stringent operation conditions of cryogenic cooling.[6–8] Nowadays, significant efforts have

*Address all correspondence to Kun Huang, khuang@lps.ecnu.edu.cn

continuously been devoted to developing high-sensitivity MIR sensors at room temperature, especially by resorting to low-dimensional materials[9–11] or novel nanophotonic structures.[12,13]

In this context, frequency upconversion detectors have emerged as an indirect yet effective approach to performing MIR detection and imaging.[14] In this approach, the infrared radiation is nonlinearly transferred to the visible or near-infrared regime, where more mature devices or techniques are available for high-performance optical manipulation and detection.[15,16] To date, such infrared upconversion detection has widely been investigated in many areas, such as free-space quantum key distribution,[17] real-time MIR optical coherence tomography,[18] or high-speed hyperspectral videography.[19–21] Generally, there are two categories for the upconversion detectors. One relies on pulsed pumping, which favors high conversion efficiency and low noise due to intense peak power and narrow time windows.[22–26] On the one hand, the involved ultrafast optical excitation enables high-precision gating in time-resolved measurement[22] and three-dimensional imaging.[24,26] On the other hand, such an active detection fashion is usually limited to cooperative targets within a relatively short capture range. In addition, the intrinsic broad spectrum for ultrashort pulses inevitably degrades the spectral resolution in upconversion infrared spectroscopy due to the convolution operation in the parametric wave-mixing process.[27,28]

Alternatively, a continuous-wave (CW) pumping scheme is employed to facilitate passive infrared sensing[29–31] and high-precision spectroscopy.[32] As the most common setting for pump sources, single-pass configuration favors great simplicity for optical alignment, yet the involved average power is typically required to be over tens of watts to implement efficient nonlinear conversion.[29,30] The use of a photonics waveguide is beneficial to reduce the required pump power,[32,33] but the single-spatial-mode confinement excludes the imaging capability. Another way to approach high pump intensity is to leverage the optical cavity enhancement technique, where the nonlinear crystal is placed within the resonating light field.[34,35] For instance, the nonlinear crystal can be directly inserted into a laser resonator to perform the so-called intracavity enhancement, which has been used to implement sensitive thermal imaging[36,37] and photon-counting ranging.[38,39] In this case, the wavelength of the involved laser diode for laser generation is usually close to the spectral band of the upconverted signal,[36] which imposes an increasing difficulty for noise suppression through spectral filtering, and typically results in an NEP of about tens of $\mathrm{fW/Hz^{1/2}}$.[40] To this end, an external-cavity enhancing scheme has been investigated to decouple the pump source and enhance the cavity, leading to improved system flexibility.[41,42] Moreover, the pump source can benefit from outstanding properties of single-frequency fiber lasers, such as compact layout, low noise, and narrow linewidth,[43] which offers great potential to implement high-fidelity MIR upconverter for high-resolution spectroscopy[32] and coherent optical communication.[33] Recently, external cavity enhancement has been adopted to demonstrate a broadband MIR upconversion spectrometer, albeit with a relatively high NEP of about a few $\mathrm{pW/Hz^{1/2}}$.[42] Therefore, it is appealing to further manifest the full potential for high-sensitivity MIR sensing by combining high-performance silicon photon counters.

Here, we implement a highly sensitive MIR upconversion detection system based on external-cavity pump enhancement, which leads to an NEP as low as 0.3 $\mathrm{fW/Hz^{1/2}}$, ~10-fold better than previously reported values for CW-pumping MIR upconversion detectors. The optical cavity is constructed with a finesse of 109, which facilitates a power-enhancing factor of up to 36. At an intracavity power of 55 W, the conversion efficiency is ~22% due to optimized spatial-mode matching among the involved optical fields within the resonator. The technical complexity of the cavity locking is mitigated using a digital locking unit based on a field-programmable gate array (FPGA), which enables automatic stabilization functionality and long-term operation. Moreover, a multi-pixel photon counter (MPPC) is used to further extend the dynamic range of the MIR upconversion detector, which indicates at least a 15-dB improvement over that of a single-pixel detector. In addition, the single-frequency pump favors high-fidelity spectral mapping, which holds great potential in sensitive and precise MIR spectroscopy.

2 Experimental Setup

Figure 1 illustrates the experimental setup for the MIR upconversion detection system based on the external-cavity pumping enhancement. The light sources are from an Er-doped fiber laser (EDFL) at 1550 nm and a Yb-doped fiber laser (YDFL) at 1064 nm. The two fiber lasers are designed to stably operate at the single-frequency regime without suffering from the mode-hopping effect.[43] The linewidth of both EDFL and YDFL is less than 3 kHz. The EDFL and YDFL deliver CW linearly polarized light at an average power of 24 and 27 mW, respectively. And the average powers are further boosted to 1 and 3 W using Er-doped and Yb-doped fiber amplifiers (EDFA and YDFA). The output of YDFA is split by a polarization beam splitter. One portion with 1-W power is spatially combined with the amplified beam from EDFA by a dichroic mirror. The mixed beam is focused into a periodically poled lithium niobate (PPLN1) crystal with a length of 50 mm to perform the difference frequency generation (DFG). The operation temperature of the crystal is stabilized at 62°C with a precision of 0.1°C, which is optimized for the poling period of 30.49 μm. The generated MIR beam at 3.4 μm is collected into a single-mode fluoride fiber (Thorlabs, Newton, New Jersey, United States, P3-32F-FC-1) with a coupling efficiency of 70%. The average power for the generated CW MIR light is ~1 mW and can be adjusted by selecting proper neutral density attenuators and varying the pumping power for the DFG.[25] The precise MIR power calibration with a large dynamic range is essential for the subsequent characterization of the sensitive upconversion detection system. The prepared MIR source is focused into a bow-tie-type standing-wave cavity by a calcium fluoride plano–convex lens (L3) with a focal length of 75 mm.

In parallel, the other portion of the YDFA serves as the pump source for the upconversion module. The pump laser is coupled into a single-mode fiber (SMF) to improve spatial mode quality and beam-steering stability. A fiber optical isolator is used to prevent returning light from disturbing or damaging the fiber laser. The pump beam is then collimated via an aspheric lens with a 7.5-mm focal length after an FC/APC fiber patch cord (Advanced Fiber Resources, Zhuhai, China, PMP-06-R-2N-L-1-S). The polarization state of the pump beam can be adjusted by rotating the half-wave and quarter-wave plates. The pump beam is mode-matched to the external cavity by optimizing the separation between the fiber end and the lens, as well as the distance between the collimator and the cavity. To perform the sum frequency generation (SFG), another nonlinear crystal (PPLN2) is used with a length of 25 mm and a poling period of 22.4 μm. The upconverted SFG light at 810 nm is steered

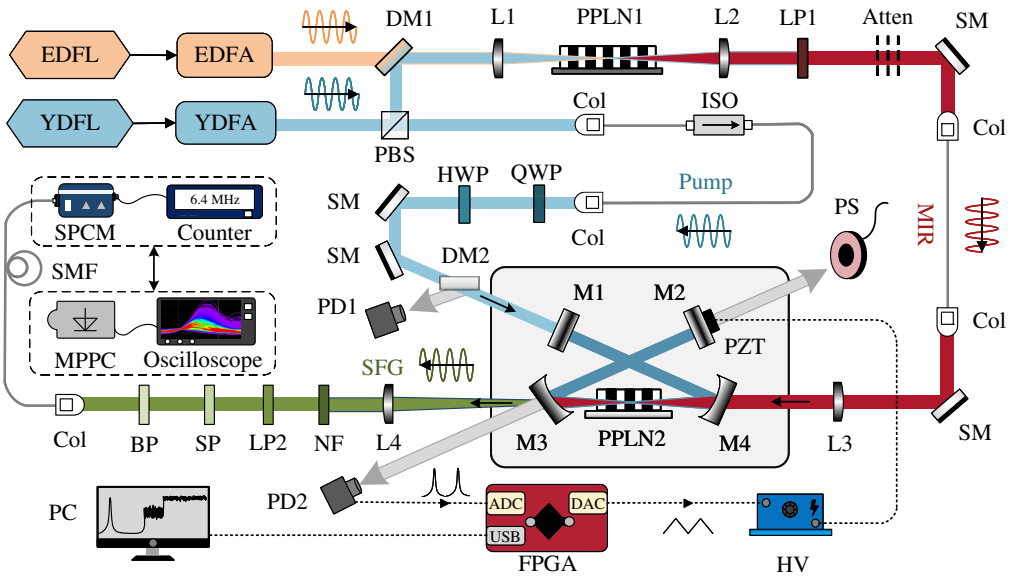

Fig. 1 Experimental setup of MIR upconversion detection based on the external-cavity pumping. An EDFL at 1550 nm and a YDFL at 1064 nm are used to provide initial light sources for subsequent nonlinear frequency conversion. The two fiber lasers, operating at the single-longitudinal mode, are first used to prepare the MIR signal at 3.4 μm based on the DFG in a PPLN1 crystal. Then, the generated MIR beam is injected into an optical cavity for implementing the sum-frequency generation. The cavity comprises four mirrors and is stabilized with a digital locking unit based on a programmed FPGA. Under the locked state, the pump power can significantly be enhanced within the cavity. After passing through a series of spectral filters, the upconverted signal is coupled into an SMF before being detected by an SPCM or an MPPC. YDFA and EDFA, Yb- and Er-doped fiber amplifiers; DM, dichroic mirror; PBS, polarization beam splitter; L, lens; Atten, attenuator; SM, silver mirror; Col, collimator; ISO, isolator; HWP and QWP, half-wave and quarter-wave plates; M, cavity mirror; PZT, piezoelectric actuator; PD, photodiode; PC, computer; HV, high-voltage amplifier; PS, power sensor; NF, notch filter; LP, SP, and BP, long-, short-, and bandpass filters.

through a spectral filtering stage that consists of a notch filter at 1064 nm with a bandwidth of 44 nm, a long-pass filter with a cut-off wavelength of 700 nm, a short-pass filter at 900 nm, and a bandpass filter with a bandwidth of 3 nm. The total transmission efficiency η_{filter} of the filtering group is ~64.8%, with a rejection ratio for the pump of ~190 dB. Finally, the filtered signal is coupled into an SMF with a coupling efficiency η_{fiber} of 80% before being recorded by a single-photon counting module (SPCM) based on a silicon avalanche photodiode with a detection efficiency η_{det} of 60%.

3 Results and Discussion

In the following, we begin with characterizing the optical cavity. Figure 2(a) presents the photograph of the implemented cavity, which consists of four mirrors on an aluminum base. Specifically, an oven is inserted within the cavity, where the crystal is placed on a copper holder. The oven is mounted on a high-precision alignment stage (Newport, California, United States, 9071-M), which allows a four-axis adjustment with a 3-mm linear movement and an 8 deg angular rotation. The compact kinematic stage facilitates the alignment of the nonlinear crystal in a precise and stable way. Notably, one mirror (M2) is mounted with a donut-shaped piezoelectric actuator (PZT, Thorlabs PA44M3KW), which gives an auxiliary port for monitoring the leaking pump. As depicted in Fig. 2(b), the resonator is integrated into an assembly of 24 cm × 13 cm × 11 cm. Mirrors M1 to M3 and M4 are made of N-BK7 and calcium fluoride, respectively. The M1 and M2 are flat mirrors, and M3 and M4 have a radius of curvature of –100 mm. The coupling mirror M1 is coated with a power reflection of 97% at 1064 nm, while the others are highly reflected. More details about mirror design are given in Table 1.

In the cavity configuration, the mirror separations are crucial for adjusting the cavity-mode size, as shown in Fig. 2(c). In our experiment, the D1 and D2 are set to be 12.5 and 5.5 cm, respectively, which results in a cavity waist of 69 μm. The tight waist is beneficial for achieving high pump intensity, while the corresponding Rayleigh length for the Gaussian mode is sufficiently long to avoid the crystal insertion loss. Figure 2(d) presents the beam-size evolution along the optical cavity. For a crystal thickness of 1 mm, the beam can propagate through the nonlinear crystal without suffering from beam truncation.

To further analyze the performance of power enhancement, a high-voltage sawtooth waveform is applied to the PZT for cavity-length sweeping. As given in Fig. 3(a), a series of resonating peaks can be observed for the pump transmission (PD2) and reflection (PD1). The uneven separation between two adjacent peaks is due to the nonlinearity of the PZT actuator. Moreover, the hysteresis behavior for the PZT is manifested by the asymmetry for the up- and down-scanning traces. Thanks to the spatial mode filtering for the pump, a nearly perfect mode matching

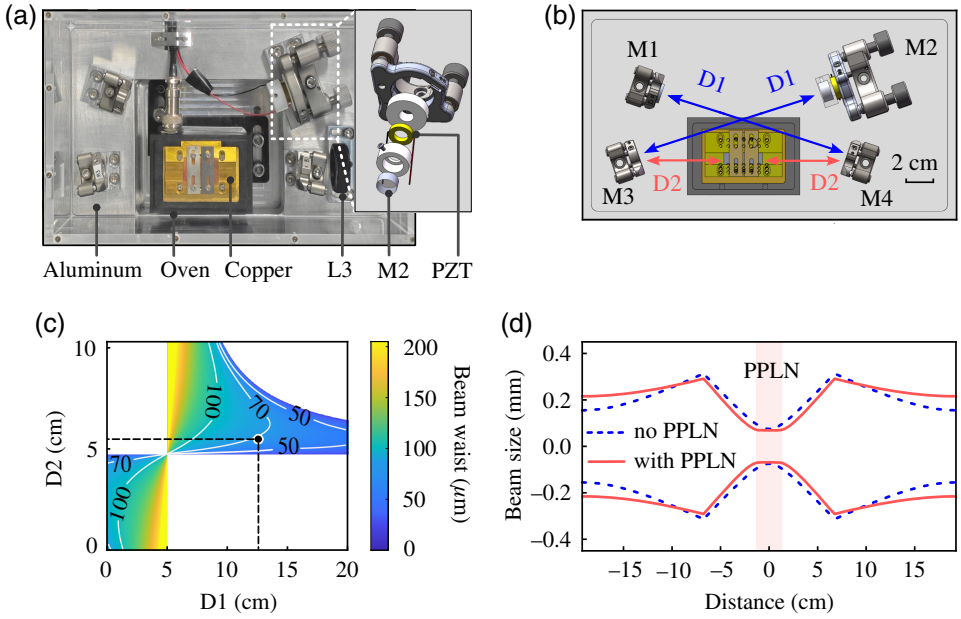

Fig. 2 (a) Photo of the enhancement optical cavity, indicating the materials of each part. (b) Physical layout of the bow-tie cavity. The distances D1 and D2 are two critical parameters for the cavity design. (c) The radius of the beam waist within the nonlinear crystal as a function of D1 and D2. The black point denotes the values used in the experiment, corresponding to a beam radius of 69 μm. Note that the area in white represents the unstable region for an optical cavity. (d) Evolution of the beam size as the light propagates along the cavity, with and without the presence of the crystal inside the cavity. The origin is defined at the center of the crystal. The shaded area indicates the occupied space by the 25-mm-length nonlinear crystal.

is achieved with negligible high-order peaks. The presence of only the fundamental mode would facilitate the cavity locking at a stable transverse mode. The cavity finesse $\mathcal{F}$ is evaluated to be ~109 from the ratio between the free spectral range and the cavity bandwidth. Note that average values for the peak separation and peak width are used to improve the estimation accuracy. The finesse is directly related to the cavity loss, as given by the following formula[34]:

$$\mathcal{F} = \frac{2\pi}{T_1 + T_2 + 2T_3 + 2T_4 + 2L}, \tag{1}$$

where T_i is the power transmission for each mirror, and L is the insertion loss for the crystal. The expression for peak intensity enhancement is given by[34]

Table 1 Parameters of the cavity mirrors.

Mirror	Material	ROC[a] (mm)	S1[b]	S2[b]
1	N-BK7	∞	PR(p)	AR(p, s, u)
2	N-BK7	∞	HR(p)	AR(p, s, u)
3	N-BK7	−100	HR(p), HT(u)	AR(p, s, u)
4	CaF_2	−100	HR(p), HT(s)	AR(p, s, u)

[a]ROC: The radius of curvature of the cavity mirror.

[b]S1 and S2 are the two surfaces of the cavity mirror. High reflection (HR), antireflection (AR), and partial reflection (PR) designations are followed by the wavelength for which the coating is designed, using the following abbreviations: pump (p, 1064 nm), signal (s, 3400 nm), and upconverted (u, 810 nm) fields.

$$\Gamma = \frac{1 - R_1}{\left(1 - \sqrt{R_1 R_2} R_3 R_4 T\right)^2}, \tag{2}$$

where R_i is the power reflectivity for each mirror, and T is the transmission for the crystal. At the approximation of a low-loss cavity, the enhancing factor is directly linked to the cavity finesse as $\Gamma \approx \mathcal{F}/\pi$. In our experiment, the enhancing factor is measured to be ~36, which is consistent with the theoretical value of 35.6. Although the standing-wave cavity is more lossy than the traveling-wave cavity, the bidirectional operation offers better immunity to the perturbation of fractional Bragg reflection from a periodically poled nonlinear crystal.[35] The standing-wave cavity layout could provide an expedient solution to obtain stabler and higher enhancement, especially in the presence of long-length crystals. In addition, the enhancement cavity is engineered to be impedance-matched, as shown by the reflection trace (PD1) in Fig. 3(b), where the transmission coefficient of the input mirror (M1) for the pump radiation matches the coefficient quantifying all other losses. Consequently, the back reflection of pump power is minimized to improve the energy utilization efficiency and to reduce the detrimental effect on the amplifier and laser.

In our experiment, the active stabilization of the external cavity is realized by a digital dither locking system based on an FPGA hardware board.[44] The FPGA is programmed to output a small-amplitude sinusoidal waveform with a frequency of 20 kHz. The dithering operation on the PZT behaves as if the laser frequency were oscillating back and forth. A digital lock-in amplifier is used to produce an error signal, as shown in Fig. 3(b). Such a digital locking system offers unique features

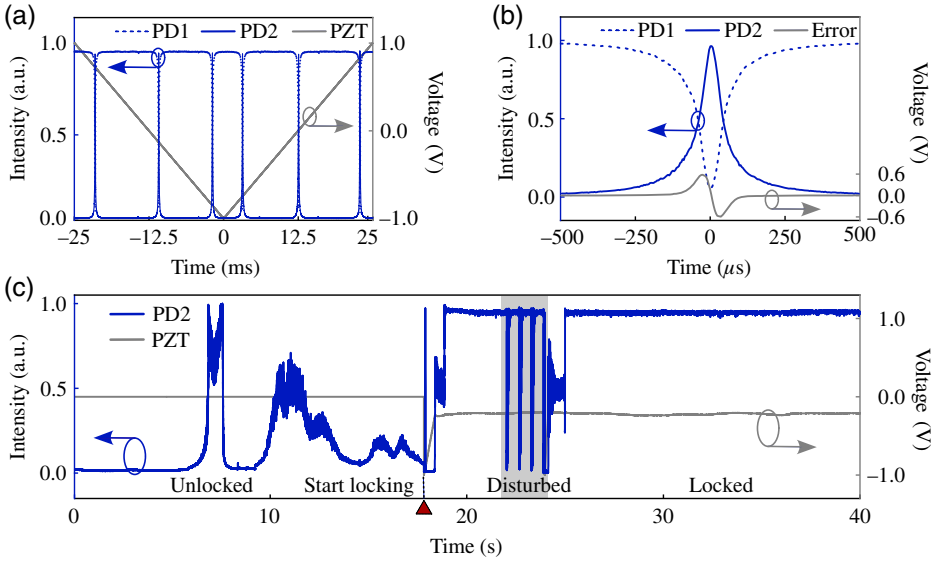

Fig. 3 (a) Recorded traces of the reflection (PD1) and transmission (PD2) lights from the optical cavity while scanning the PZT at a rate of 20 Hz. The peaks correspond to the resonating points for the fundamental spatial mode. (b) Enlarged illustration for the peak, along with the error signal for the dither locking. (c) Measured intensity for the cavity transmission during the stabilization process. The locking is engaged at 18 s, as indicated by the red triangle. The presented disturbing drops are ascribed to the intentional perturbation for testing the re-locking feature of the digital feedback unit.

of state monitoring and automatic operation. Figure 3(c) illustrates a representative process from unlocked to locked states. The several disturbing drops are ascribed to the intentional perturbation, which indicates a fast re-locking capability. When the cavity is locked at the resonance for an injection pump power of 1.53 W, the circulating power in the cavity is inferred to be ~55 W from the pump leakage out of the cavity mirror (M2). The power fluctuation of the enhanced pump light is estimated to be ~1%, which is essential for the implementation of a high-stability frequency upconverter.

Now, we turn to investigate the performance of the MIR upconversion detector. Figure 4(a) shows the measured dependence of the SFG intensity on the operating temperature of the nonlinear crystal, which agrees with the theoretical simulation under the assumption of plane-wave interaction. With the 22.4-μm grating period of the PPLN crystal, the phase-matching temperature is identified to be 102.6°C. Figure 4(b) shows the beam profile of the upconverted light when the optical cavity is locked at the resonance to the pump light. The cross sections along the two orthogonal directions indicate a superior Gaussian spatial mode confined by the optical resonator. The high beam quality of the pump field not only improves the conversion efficiency due to the improved spatial overlap among interacting fields but also facilitates subsequent coupling into an SMF for suppressing background noises. Under the approximation of non-depleted pumping, the conversion efficiency is defined by the photon-flux ratio between the SFG and MIR light, which is expressed as

$$\eta_{\text{conv}} = \frac{P_u}{P_s} \times \frac{\lambda_u}{\lambda_s}, \tag{3}$$

where λ_u and λ_s are the wavelengths for SFG and MIR lights, and P_u and P_s denote the measured average powers for the two fields. As shown in Fig. 4(c), the conversion efficiency is increased with a higher intracavity power. Correspondingly, the peak total detection efficiency for the MIR signal is evaluated to ~6.8% according to $\eta_{\text{total}} = \eta_{\text{conv}} \times \eta_{\text{filter}} \times \eta_{\text{fiber}} \times \eta_{\text{det}}$.

Another key parameter for an optical detector is the background noise, which is measured by blocking the MIR signal before the upconversion detector. As shown in Fig. 4(d), the background noise linearly increases as the pump power is augmented. The photon count of the noise N_{BG} is measured to be 78 kHz at an intracavity power of 55 W. The background noise is mainly due to the upconverted light of the spontaneous parametric downconversion fluorescence.[40] For a photon-counting detector, the detection sensitivity is usually defined by the NEP[25,40],

$$\sigma_{\text{NEP}} = \frac{E\sqrt{2N_{\text{BG}}}}{\eta_{\text{total}}}, \tag{4}$$

where E represents the photon energy of the MIR signal. As shown in Fig. 4(d), the σ_{NEP} tends to saturate for high pump powers. The achieved minimum NEP is ~0.3 fW/Hz$^{1/2}$, which is at least 1 order of magnitude better than reported values in various configurations, as listed in Table 2. It can be seen that our scheme not only provides a high conversion efficiency due to the significant pump enhancement but also exhibits a high detection sensitivity due to effective noise suppression. Compared with the intracavity scheme, the presented approach can in principle support a higher enhancing factor due to many fewer elements in the cavity. With the help of further loss reduction, the intracavity pump power up to 400 W is feasible with an enhancing factor of up to 100.[42] Another unique feature of the external-cavity enhancement is the exclusion of the laser pump at a wavelength close to the SFG signal, which leads to a much

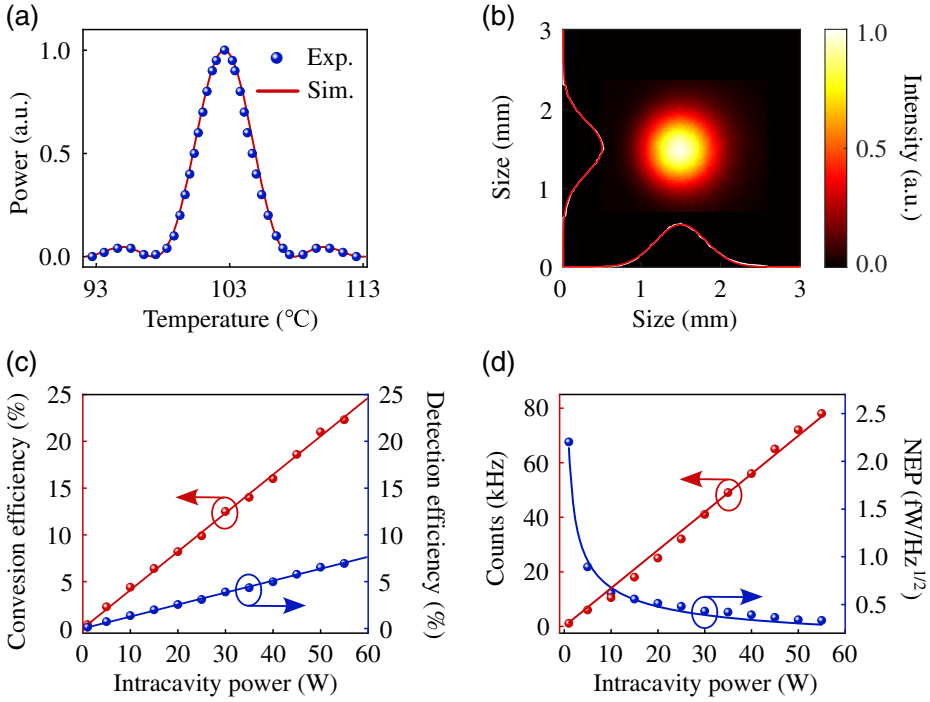

Fig. 4 (a) SFG power as a function of crystal temperature. (b) Captured beam profile for the SFG light. (c) Intrinsic conversion efficiency and total detection efficiency increase as augmenting the intracavity power. (d) Measured background count and NEP as a function of the intracavity power.

Table 2 Performance comparison for CW-wave pumping MIR upconversion detection systems.

Ref.	Scheme	Wavelength (μm)	NEP (fW/Hz$^{1/2}$)	Conversion efficiency (%)
This study	External cavity	3.4	0.3	22
42	External cavity	3.7 to 4.7	700 to 10,000	~0.001
30	Single pass	4.6	3.24	8.87
31	Single pass	4.15	/[a]	0.18
29	Single pass	10.6	4000	20
36	Intracavity	3	/[b]	20
40	Intracavity	3.4	20	6
37	Intracavity	3	/[c]	28[d]
39	Intracavity	3	161[e]	2

[a]The minimum detectable incoherent MIR power of the system is 813 fW, but the NEP is not specified.

[b]The dark noise is 0.2 photons/spacial element/second when operating at room temperature, and the camera used has 200×100 resolvable image elements. The system detection efficiency is not specified.

[c]The minimum detectable incoherent MIR power of the system is 31 fW, but the NEP is unspecified.

[d]The conversion efficiency per watt of pump power is comparable to our work.

[e]The NEP is inferred from the given values with a background noise of 8.5 MHz and a system detection efficiency of 0.15%.

lower background noise. We note that the upconverted thermal emission also contributes to the background noise, which is particularly pronounced for operation wavelengths above 3 μm due to the increased linear absorption for the PPLN crystal.[40] The thermal noise can be suppressed by reducing the crystal temperature at an optimized poling period for phase matching.

Finally, we have adopted a silicon MPPC for extending the detection dynamic range for the MIR upconversion detector. In contrast to the single-pixel photon counter, the MPPC offers a unique capability of photon-number-resolving (PNR) detection.[25] The MPPC (Hamamatsu Photonics, Hamamatsu-city, Japan, S13362-3050DG) comprises 60 pixel $\times$ 60 pixel on an effective active area of 9 mm^2. The PNR detection is realized via spatial multiplexing, where incident photons could be registered by different pixels. The detection efficiency η_{MPPC} MPPC was ~7% at 810 nm, which can be further improved by resorting to an MPPC with a larger pixel pitch and a higher fill factor. To better characterize the detector performance, a pulsed MIR source is prepared by inserting an electro-optic modulator (not shown in Fig. 1) at the output of EDFL, which generates a pulse duration of 1 ns at a repetition rate of 10 MHz. As shown in Fig. 5, the photon-counting rate for the SPCM is saturated as the incident power increases, which results in a dynamic range of 15 dB. In comparison, the MPPC offers a dynamic range of up to 30 dB. Notably, the MPPC typically has a large detection area, which favors a high collection efficiency for the upconverted signal in the free-space configuration. The achieved MIR detection performance with single-photon sensitivity and large dynamic range would facilitate a variety of applications, such as free-space communication, trace molecule spectroscopy, and long-range infrared sensing.

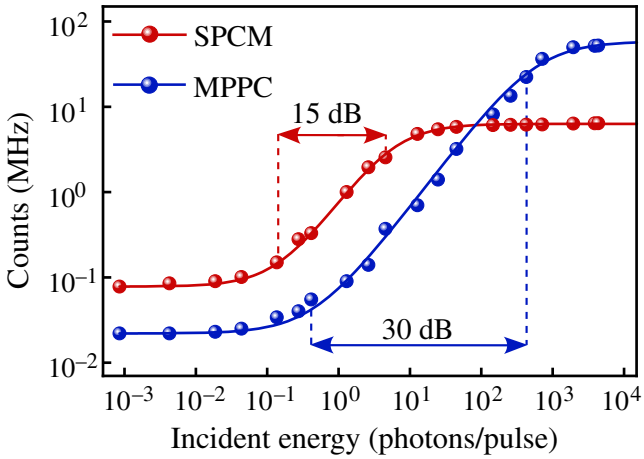

Fig. 5 Measured photon counts varying with the incident power is increased in two cases of using optical detectors based on SPCM and MPPC, which indicate detection dynamic ranges of 15 and 30 dB in the linear response regime, respectively. The solid lines are fitted to guide the eyes.

4 Conclusion

In conclusion, we have implemented an ultrasensitive MIR upconversion detection system with high conversion efficiency and low background noise. The operation wavelength can cover an MIR spectral range from 3 to 5 μm defined by the transparency window of the PPLN crystal. The demonstrated sensitivity is at least 2 orders of magnitude better than those of conventional detectors based on PbS, PbSe, and HgCdTe.[4,9] In comparison to single-pass schemes,[29–31] the involved nonlinear converter is constructed based on the external optical cavity, which favors pump-power enhancement, spatial-mode confinement, and parametric noise suppression. Moreover, the presented configuration favors a reduced cavity loss due to fewer optical elements, which can in principle access high enhancing factors that are beyond the reach of the intracavity scheme.[39,40] Notably, the separation arrangement of the laser and enhancement cavities allows one to adopt the compact single-frequency fiber lasers and amplifiers,[43] which circumvents the complexity of spectral engineering in solid-state lasers. Such narrowband pumping is essential for achieving high-fidelity spectral mapping, which is particularly attractive for high-precision molecular spectroscopy.[32] In this scenario, our MIR upconversion detector can be modified to obtain a large spectral coverage using nonlinear crystals with fanout[45] or chirped poling[46,47] structures. In addition, the operation window is possible to extend into longer infrared wavelengths up to 12 μm with $BaGa_4Se_7$[48] or $AgGaS_2$[49] crystals. It is worth noting that the presented architecture is readily adapted to realize upconversion MIR imaging.[15,36]

Disclosures

The authors declare no competing interests.

Code and Data Availability

The data that support the findings of this study are available from the corresponding author upon reasonable request.

Acknowledgments

This work was supported by the National Key Research and Development Program (Grant No. 2021YFB2801100), the National Natural Science Foundation of China (Grant Nos. 62175064, 62235019, 62035005, and 12022411), the Shanghai Pilot Program for Basic Research (Grant No. TQ20220104), the Natural Science Foundation of Chongqing (Grant Nos. CSTB2023NSCQ-JQX0011, CSTB2022NSCQ-MSX0451, and CSTB2022NSCQ-JQX0016), the Shanghai Municipal Science and Technology Major Project (Grant No. 2019SHZDZX01), and the Fundamental Research Funds for the Central Universities.

References

1. K. L. Vodopyanov, *Laser-Based Mid-Infrared Sources and Applications*, Wiley (2020).
2. M. Razeghi and B. M. Nguyen, "Advances in mid-infrared detection and imaging: a key issues review," *Rep. Prog. Phys.* **77**, 082401 (2014).
3. R. H. Hadfield et al., "Single-photon detection for long-range imaging and sensing," *Optica* **10**, 1124–1141 (2023).
4. S. D. Russo et al., "Advances in mid-infrared single-photon detection," *Photonics* **9**, 470 (2022).
5. Y. Fang et al., "Mid-infrared photonics using 2D materials: status and challenges," *Laser Photonics Rev.* **14**, 1900098 (2020).
6. G. G. Taylor et al., "Low-noise single-photon counting superconducting nanowire detectors at infrared wavelengths up to 29 μm," *Optica* **10**, 1672–1678 (2023).
7. Y. Pan et al., "Mid-infrared Nb_4N_3-based superconducting nanowire single photon detectors for wavelengths up to 10 μm," *Opt. Express* **30**, 40044–40052 (2022).
8. Q. Chen et al., "Mid-infrared single photon detector with superconductor $Mo_{0.8}Si_{0.2}$ nanowire," *Sci. Bull.* **66**, 965–968 (2021).
9. P. Wang et al., "Sensing infrared photons at room temperature: from bulk materials to atomic layers," *Small* **15**, 1904396 (2019).
10. J. Wu et al., "Emerging low-dimensional materials for mid-infrared detection," *Nano Res.* **14**, 1863–1877 (2021).
11. X. Xue et al., "High-operating-temperature mid-infrared photodetectors via quantum dot gradient homojunction," *Light Sci. Appl.* **12**, 2 (2023).
12. A. Xomalis et al., "Detecting mid-infrared light by molecular frequency upconversion in dual-wavelength nanoantennas," *Science* **374**, 1268–1271 (2021).
13. W. Chen et al., "Continuous-wave frequency upconversion with a molecular optomechanical nanocavity," *Science* **374**, 1264–1267 (2021).
14. A. Barh et al., "Parametric upconversion imaging and its applications," *Adv. Opt. Photonics* **11**, 952–1019 (2019).
15. K. Huang et al., "Wide-field mid-infrared single-photon upconversion imaging," *Nat. Commun.* **13**, 1077 (2022).
16. X. Zeng et al., "Tunable mid-infrared detail-enhanced imaging with micron-level spatial resolution and photon-number resolving sensitivity," *Laser Photonics Rev.* **17**, 2200446 (2023).
17. S. K. Liao et al., "Long-distance free-space quantum key distribution in daylight towards inter-satellite communication," *Nat. Photonics* **11**, 509–513 (2017).
18. N. M. Israelsen et al., "Real-time high-resolution mid-infrared optical coherence tomography," *Light Sci. Appl.* **8**, 11 (2019).
19. S. Junaid et al., "Video-rate, mid-infrared hyperspectral upconversion imaging," *Optica* **6**, 702–708 (2019).
20. Y. Zhao et al., "High-speed scanless entire bandwidth mid-infrared chemical imaging," *Nat. Commun.* **14**, 3929 (2023).
21. J. Fang et al., "Wide-field mid-infrared hyperspectral imaging beyond video rate," *Nat. Commun.* **15**, 1811 (2024).

22. S. Wolf et al., "Self-gated mid-infrared short pulse upconversion detection for gas sensing," *Opt. Express* **25**, 24459–24468 (2017).
23. A. S. Ashik et al., "Mid-infrared upconversion imaging using femtosecond pulses," *Photonics Res.* **7**, 783–791 (2019).
24. P. Rehain et al., "Noise-tolerant single photon sensitive three-dimensional imager," *Nat. Commun.* **11**, 921 (2020).
25. K. Huang et al., "Mid-infrared photon counting and resolving via efficient frequency upconversion," *Photonics Res.* **9**, 259–265 (2021).
26. J. Fang et al., "Mid-infrared single-photon 3D imaging," *Light Sci. Appl.* **12**, 144 (2023).
27. T. Zheng et al., "High-speed mid-infrared single-photon upconversion spectrometer," *Laser Photonics Rev.* **17**, 2300149 (2023).
28. B. Sun et al., "Single-photon time-stretch infrared spectroscopy," *Laser Photonics Rev.* **18**, 2301272 (2024).
29. R. Demur et al., "High sensitivity narrowband wavelength mid-infrared detection at room temperature," *Opt. Lett.* **42**, 2006–2009 (2017).
30. Y. Li et al., "Ultra-sensitive mid-wavelength-infrared upconversion detector," *Opt. Laser Technol.* **168**, 109993 (2024).
31. Z. Ge et al., "Midinfrared up-conversion imaging under different illumination conditions," *Phy. Rev. Appl.* **20**, 054060 (2023).
32. T. W. Neely et al., "Broadband mid-infrared frequency upconversion and spectroscopy with an aperiodically poled $LiNbO_3$ waveguide," *Opt. Lett.* **37**(20), 4332–4334 (2012).
33. K. D. F. Büchter et al., "All-optical Ti:PPLN wavelength conversion modules for free-space optical transmission links in the mid-infrared," *Opt. Lett.* **34**, 470–472 (2009).
34. M. F. Witinski, J. B. Paul, and J. G. Anderson. "Pump-enhanced difference-frequency generation at 3.3 μm," *Appl. Opt.* **48**, 2600–2606 (2009).
35. K. Huang et al., "Observation of spectral mode splitting in a pump-enhanced ring cavity for mid-infrared generation," *Opt. Express* **27**, 11766–11775 (2019).
36. J. S. Dam, P. Tidemand-Lichtenberg, and C. Pedersen, "Room-temperature mid-infrared single-photon spectral imaging," *Nat. Photonics* **6**, 788–793 (2012).
37. N. Huang et al., "Femtowatt incoherent image conversion from mid-infrared light to near-infrared light," *Laser Phys.* **27**, 035401 (2017).
38. W. Yue et al., "Eye-safe aerosol and cloud lidar based on free-space intracavity upconversion detection," *Remote Sens.* **14**, 2934 (2022).
39. M. Widarsson et al., "Room temperature photon-counting lidar at 3 μm," *Appl. Opt.* **61**, 884–889 (2022).
40. R. L. Pedersen et al., "Characterization of the NEP of mid-infrared upconversion detectors," *IEEE Photonics Technol. Lett.* **31**, 681–684 (2019).
41. M. A. Albota and N. C. W. Franco, "Efficient single-photon counting at 1.55 μm by means of frequency upconversion," *Opt. Lett.* **29**, 1449–1451 (2004).
42. S. Wolf et al., "Upconversion-enabled array spectrometer for the mid-infrared, featuring kilohertz spectra acquisition rates," *Opt. Express* **25**, 14504–14515 (2017).
43. S. Fu et al., "Review of recent progress on single-frequency fiber lasers," *J. Opt. Soc. Am. B* **34**, A49–A62 (2017).
44. L. Neuhaus et al., "PyRPL (Python Red Pitaya Lockbox)—an open-source software package for FPGA-controlled quantum optics experiments," in *Conf. Lasers and Electro-Opt. Eur. Eur. Quantum Electron. Conf. (CLEO/Europe-EQEC)* (2017).
45. A. Barh et al., "Upconversion spectral response tailoring using fanout QPM structures," *Opt. lett.* **44**, 2847–2850 (2019).
46. S. M. M. Friis and L. Høgstedt, "Upconversion-based mid-infrared spectrometer using intra-cavity $LiNbO_3$ crystals with chirped poling structure," *Opt. lett.* **44**, 4231–4234 (2019).
47. M. Mrejen et al., "Multicolor time-resolved upconversion imaging by adiabatic sum frequency conversion," *Laser Photonics Rev.* **14**, 2000040 (2020).
48. P. Liu et al., "Large dynamic range and wideband mid-infrared upconversion detection with $BaGa_4Se_7$ crystal," *Optica* **9**, 50–55 (2022).
49. P. J. Rodrigo et al., "Room-temperature, high-SNR upconversion spectrometer in the $6-12$ μm region," *Laser Photonics Rev.* **15** 2000443 (2021).

Biographies of the authors are not available.